PAPER • OPEN ACCESS

Chromatic effect in a novel THz generation scheme

To cite this article: Bin Li *et al* 2017 *New J. Phys.* **19** 113025

New Journal of Physics
The open access journal at the forefront of physics

Deutsche Physikalische Gesellschaft DPG
IOP Institute of Physics

Published in partnership with: Deutsche Physikalische Gesellschaft and the Institute of Physics

OPEN ACCESS

RECEIVED
25 February 2017

REVISED
8 July 2017

ACCEPTED FOR PUBLICATION
28 July 2017

PUBLISHED
16 November 2017

PAPER

Chromatic effect in a novel THz generation scheme

Bin Li[1,2,6], **Wenyan Zhang**[1], **Xiaoqing Liu**[1], **Haixiao Deng**[1], **Taihe Lan**[1], **Bo Liu**[1], **Jia Liu**[3], **Xingtao Wang**[1], **Zhinan Zeng**[4,6] **and Lijian Zhang**[5]

[1] Shanghai Institute of Applied Physics, Chinese Academy of Sciences, 2019 Jialuo Road, Shanghai 201800, People's Republic of China
[2] School of Physical Science and Technology, ShanghaiTech University, 100 Haike Road, Shanghai 200031, People's Republic of China
[3] European XFEL GmbH, Holzkoppel 4, D-22869 Schenefeld, Germany
[4] Laboratory for High Intensity Optics, Shanghai Institute of Optics and Fine Mechanics, Chinese Academy of Sciences, 390 Qinghe Road, Shanghai 201800, People's Republic of China
[5] National Laboratory of Solid State Microstructures and College of Engineering and Applied Sciences, Nanjing University, Nanjing 210093, People's Republic of China
[6] Author to whom any correspondence should be addressed.

E-mail: libin1995@sinap.ac.cn **and** zhinan_zeng@mail.siom.ac.cn

Keywords: terahertz radiation, optical rectification, nonlinear optics and parametric processes, optical chirp pulse, pulse-front tilt

Abstract

Deriving single or few cycle terahertz (THz) pulse by an intense femtosecond laser through cascaded optical rectification is a crucial technique in cutting-edge time-resolved spectroscopy to characterize micro-scale structures and ultrafast dynamics. Due to the broadband nature of the ultrafast driving laser, the chromatic effect limits the THz conversion efficiency in optical rectification crystals, especially for those implementing the pulse-front tilt scheme, e.g. lithium niobate (LN) crystal, has been prevalently used in the past decade. In this research we developed a brand new type of LN crystal utilizing Brewster coupling, and conducted systematically experimental and simulative investigation for the chromatic effect and multi-dimensionally entangled parameters in THz generation, predicting that an extreme conversion efficiency of ~10% would be potentially achievable at the THz absorption coefficient of ~0.5 cm^{-1}. Moreover, we first discovered that the chirp of the driving laser plays a decisive role in the pulse-front tilt scheme, and the THz generation efficiency could be enhanced tremendously by applying an appropriate chirp.

1. Introduction

THz wave spans the frequency range of 0.1–10 THz, associated with wavelength of 30 μm–3 mm, representing the most extraordinary characteristics in the overall electro-magnetic spectrum. During the past decade, THz technology and applications have developed rapidly, and are widely used in material characterization, molecular imaging and structural tomography, investigation of electron–phonon interaction and dynamics, non-destructive bio-medical diagnostics etc [1–8]. Numerous novel ideas and delicate experimental techniques are proposed and established to generate and detect THz waves [9–11]. Among them, the optical rectification has been demonstrated to create THz pulses most efficiently, through applying the ultrafast laser to induce different frequency generation (DFG) in the THz photonic crystal [12–16]. In recent years, lithium niobate (LN), either in its stoichiometric or congruent crystalline form, turns into preferable THz generation media due to its large optical-to-THz conversion efficiency, compared to many others, e.g. GaAs, ZnTe, GaP and etc [17–19]. However, an instant drawback of using LN is that its optical refractive index of far-infrared spectrum (including THz) is very different to that of the near-infrared and visible band. Thus the phase-matching between the driving laser and THz wave is not straightforwardly achieved, which limits the THz generation efficiency. The Cherenkov radiation scheme is then adopted and demonstrated to enhance the THz generation efficiency remarkably, where the laser pulse front is tilted purposely with respect to its propagation direction [20–24]. Thus DFG takes place within the intra-band of the laser pulse through a non-collinear geometry, where the generated THz wave is expected to propagate towards the pulse-front of the driving pulse.

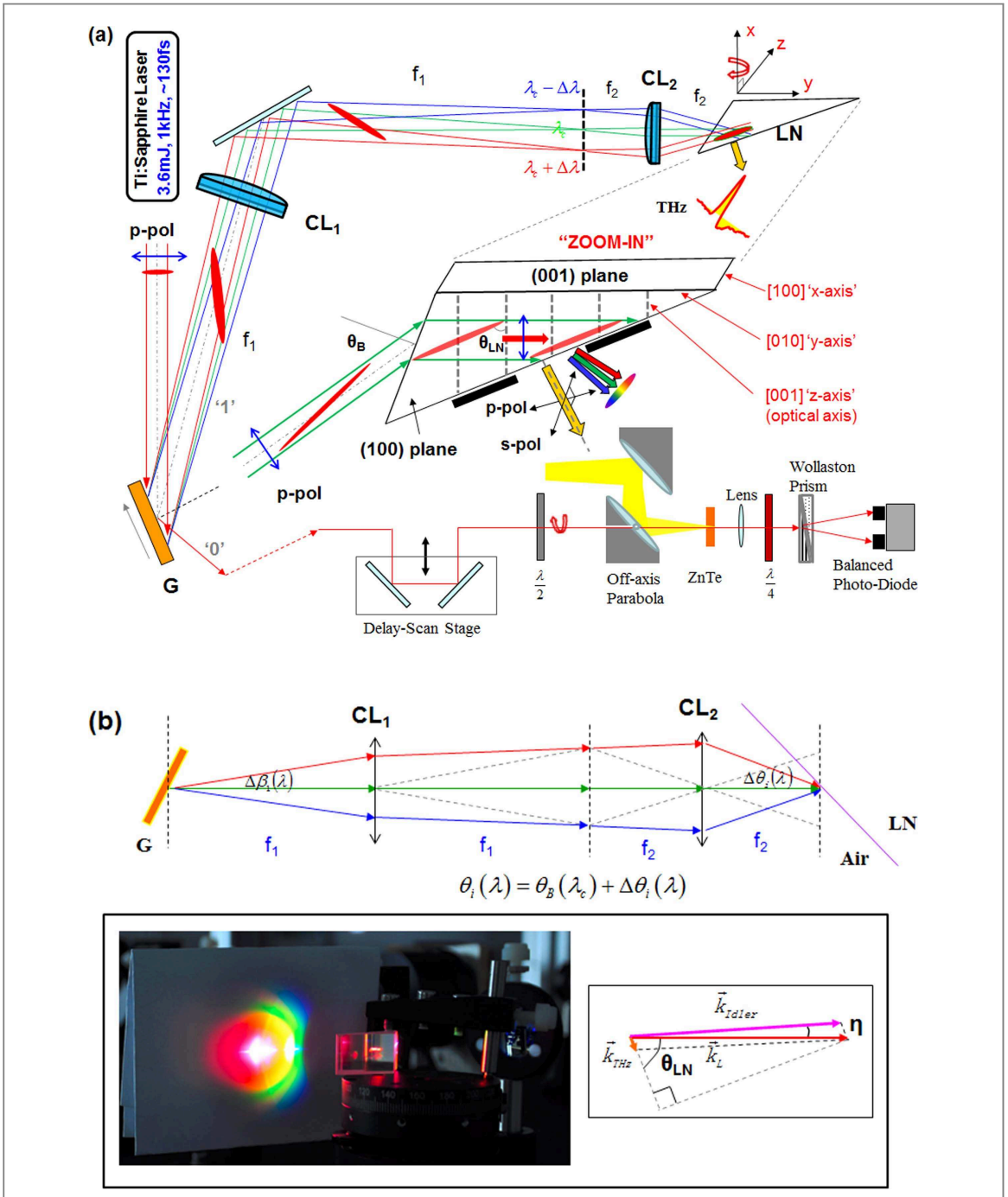

Figure 1. (a) The schematic layout of the THz generation setup ('bird's-eye view'), implementing the pulse-front tilt scheme through Brewster incidence coupling. The '1' order of the grating (G)—'diffraction beam' possessing pulse-front tilt is used to derive THz wave in the LN crystal, and the '0' order—'reflection beam' is used as probe to characterize the THz field in time domain through EO sampling technique. The diffraction beam is delivered through a pair of cylindrical lenses (CL_1/CL_2) to obtain a desired demagnification of f_1/f_2 in its tangential coordinate before being fed into LN. The center of the figure shows the 'zoomed-in' 3D feature of the pulse-front tilted driving beam propagation through the LN crystal, where the yellow arrow in the middle indicates the THz beam while the colored arrows next to it represent the residual driving beam escaping from the crystal after several times of the internal reflection. (b) The chromatic effect of the driving beam is shown, where various intra-band wavelengths are associated with different optical paths, in-between the grating and LN crystal, via the de-collimation lens-pair (top-view). The photograph and vector diagram illustrate, respectively, the IR driving pulse spectral broadening feature accompanying THz generation in the crystal and the phase matched non-collinear DFG process achieving high 'optical-to-THz' conversion efficiency (see text).

The pulse-front tilt scheme for THz generation in LN is illustrated in figure 1, where a photon of the driving laser $\vec{k}\,(\omega_L)$ is decomposed into photons of THz $\vec{k}\,(\Omega_{\mathrm{THz}})$ and idler $\vec{k}\,(\omega_L - \Omega_{\mathrm{THz}})$. And the process could be cascaded multiple times (refer to equation (1)), so the ultimate photon energy of the residual driving beam would be significantly smaller than its initial value (up to a few tens of terahertz), displaying apparent 'red-shift' broadening spectral features (refer to figure 4(a)) [12, 13].

$$\begin{cases} \vec{k}(\omega_L) = \vec{k}(\omega_L - \Omega_{\mathrm{THz}}) + \vec{k}(\Omega_{\mathrm{THz}}) \\ \vec{k}(\omega_L - \Omega_{\mathrm{THz}}) = \vec{k}(\omega_L - 2\Omega_{\mathrm{THz}}) + \vec{k}(\Omega_{\mathrm{THz}}) \\ \vec{k}(\omega_L - 2\Omega_{\mathrm{THz}}) = \vec{k}(\omega_L - 3\Omega_{THz}) + \vec{k}(\Omega_{\mathrm{THz}}) \\ \cdots \quad \cdots \end{cases}. \tag{1}$$

The phase (or wave vector) match condition between the laser and THz wave through the non-collinear coupling scheme in figure 1 determines the optimal pulse-front tilt angle for the driving beam in LN,

$$\Delta\vec{k} = \vec{k}(\Omega_{\mathrm{THz}}) + \vec{k}(\omega_L - \Omega_{\mathrm{THz}}) - \vec{k}(\omega_L) = 0. \tag{2}$$

Thus

$$\begin{aligned} |\Delta\vec{k}| &\approx \frac{\Omega_{\mathrm{THz}} \cdot n(\Omega_{\mathrm{THz}})}{c} \cos\theta_{\mathrm{LN}} - \left(\frac{\mathrm{d}k}{\mathrm{d}\omega}\right)_L \cdot \Omega_{\mathrm{THz}} \\ &= \frac{\Omega_{\mathrm{THz}}}{c}[n(\Omega_{\mathrm{THz}})\cos\theta_{\mathrm{LN}} - n_g(\omega_L)] = 0, \end{aligned} \tag{3}$$

which leads to [23]

$$\theta_{\mathrm{LN}} = \cos^{-1}\left(\frac{n_g(\omega_L)}{n(\Omega_{\mathrm{THz}})}\right), \tag{4}$$

where $n_g(\omega_L)$ and $n(\Omega_{\mathrm{THz}})$ are the group index of the driving laser, and the phase index of THz wave respectively. As shown in the figure, the optimal tilt angle θ_{LN} is actually the desired intersect angle between the propagation directions of the laser and THz wave. While the THz wave propagates a distance of L, parallel to the pulse-front normal of the driving laser, the laser pulse would propagate a distance of $L/\cos\theta_{\mathrm{LN}}$ in the meantime [21–25]. The chromatic effect of the driving beam is demonstrated in figure 1(b), where various intra-band wavelengths of the ultrafast optical laser are associated with different optical paths between the grating and LN crystal, relayed by a pair of tangential de-collimation lens-pair.

2. Experiment and simulation

2.1. Experimental apparatus

Compared to the typical pulse-front tilt scheme previously used for THz generation in LN, through applying pump laser beam with vertical polarization (s-pol) to incident on a side plane of a horizontal '*z*-cut' crystal [20–26], the major difference and advantage of our setup is that the LN crystal is in the presence of both a *horizontal* '*x*-cut' and *vertical* '*z*-cut', where a laser beam with horizontal polarization (p-pol) incidents onto a side plane, approaching Brewster's angle to reduce the Fresnel loss at the 'air–LN' interface (figure 1). The unique double-face-cut LN crystal is shaped in a triangular prism and congruently doped with MgO of 6.0% molecular concentration, with dimensions of 15.5 mm × 22.4 mm (*Y*) × 32.1 mm in cross-section and a height of 15.0 mm (*X*), fabricated by United Crystal Inc., USA through customer request. Upon Brewster's incidence at a side surface of 15.5 mm × 15.0 mm(*X*), the refractive laser beam would propagate along the *y*-axis after entering into the crystal with polarization remaining parallel to the *z*-axis (optical axis), to ensure the THz generation efficiency.

The driving pulse is provided by a conventional Ti:Sapphire laser system (Coherent Legend Duo regenerative laser amplifier), with repetition rate of 1 kHz, pulse energy up to ~3.6 mJ, FWHM bandwidth of ~7.6 nm center at 800 nm, and pulse duration of ~130 fs, corresponding to a transform-limit (TL) pulse of nearly full coherence. The laser beam with ~5 mm diameter incidents on a blazing type plane grating with groove density of 2200 ln mm^{-1} optimally blazed at 800 nm, to create the desired pulse-front tilt. The p-polarized laser beam incidents at an angle of 65° respected to the grating normal, thus the '1' order diffraction beam is outgoing at ~58.6°. This 'Littrow' approaching incidence–diffraction geometry could achieve diffraction efficiency beyond ~90%. The beam is further delivered through a pair of cylindrical lenses, CL_1 ($f_1 = 300$ mm) and CL_2 ($f_2 = 100$ mm), which are curved horizontally but flat vertically. Thus the diffractive beam is focused twice sequentially in its dispersive (horizontal) coordinate with moderate divergence in non-dispersive (vertical) coordinate. The lens-pair forming well-coupled 'f_1–f_1–f_2–f_2' geometry is precisely aligned to reduce the optical aberration of the driving beam, where the front focal spot of CL_1 is located at the surface of the grating (G), the rear focal spot of CL_1 is overlapped with the front focus of CL_2, and the chromatic-dispersed beam would refocus at the rear focus of CL_2 (located inside the LN crystal). The LN crystal is on a crystal mount with translational mechanism in the '*y*–*z* plane' and rotational mechanism around the '*x*-axis' (refer to figure 1). The in-plane motion could change the laser propagation length in the crystal for the THz generation, and also alter the driving beam fluence through adjusting the position of LN back and forth towards the beam focus. The rotation could fine adjust the crystal orientation in the *y*–*z* plane to achieve the desired phase match angle.

Therefore, the coordinates of LN could be well optimized for the THz generation at various driving pulse parameters.

Upon entering the LN crystal, the refractive beam would possess optimal pulse-front tilt angle of ~64°. The generated THz pulse would propagate perpendicular to the pulse-front of the driving beam, and eventually exit in normal from the largest side plane of the LN prism (32.1 mm × 15.0 mm (*X*)), where its pulse energy is measured by a pyroelectric detector with proper THz filters and beam chopper (1–50 Hz chopping rate), and cross-calibrated by a Golay Cell (both from Microtech Instrument Inc., USA). The temporal waveform of THz pulse is detected by a home-made electro-optical (EO) sampling apparatus separately [11, 14]. The weak '0'-order of the grating is used as the probe beam, passing through a delay-scan stage to change the mutual delay respected to the THz pulse, which is refocused by a couple of 90° off-axis parabola (OAP) to achieve the best focal spot in a thin ZnTe crystal. The 2nd OAP is centrally holed to allow the probe beam pass through and overlap with the THz pulse spatially and temporally at the ZnTe crystal. The probe beam then sequentially transmits a best-form focal lens, a quarter wave-plate ($\lambda/4$), a Wollaston prism, and finally splits and hits into a balanced photo-diode (PD). The EO signal from the balanced PD is phase-retrieved and recorded by a lock-in amplifier which is triggered by the synchronization signal of the laser system at 1 kHz repetition rate. In a typical EO-sampling measurement, the 'scan-delay-step' is set as 1.5 μm with 1024 steps in total, associated with the temporal resolution of ~10 fs and a timing window of ~10 ps, which could characterize the THz waveform with high temporal resolution.

2.2. Simulations for various grating groove densities and intra-band chromatic distribution of the driving pulse

As illustrated in figure 2(a), a blazing type grating with groove spacing of d_0, optimally blazed at the central wavelength $\lambda_c \sim 800$ nm is proposed working at the incidence angle of $\beta_0 \approx \theta_{\mathrm{Litt}} + 3°$, thus the diffraction beam (with diffraction angle $\beta_1(\lambda)$) would present a tilt angle for its pulse-front, according to,

$$\tan\theta_G(\lambda) = \frac{\lambda}{d_0 \cdot \cos[\beta_1(\lambda)]} = \frac{\lambda}{d_0\sqrt{1-\left(\frac{\lambda}{d_0} - \sin\beta_0\right)^2}}. \tag{5}$$

The beam is then delivered through a pair of de-magnification cylindrical lens (CL_1 and CL_2), with focal lengths of f_1 and f_2 respectively in the tangential coordinate ($f_1 > f_2$). For the monochromatic approximation, the diffractive beam size would effectively decreases f_2/f_1 at the rear focal spot of CL_2 (located inside the LN crystal). Implementing the parameters of the optical layout in figure 1, the expected pulse-front tilt angle of the driving beam in the LN crystal could be described as,

$$\tan\theta_{\mathrm{LN}}(\lambda) = \frac{\tan\theta_G(\lambda)}{n_g(\lambda)}\frac{\cos\theta_i(\lambda)}{\cos\theta_t(\lambda)}\frac{f_1}{f_2}, \tag{6}$$

where θ_i (set to Brewster's angle θ_B at λ_c) and θ_t are the incidence and refraction angle of the laser beam at the air-LN interface. The result of θ_{LN} given by equation (6) should be equal to that in equation (4), thus the de-magnification of f_1/f_2 could be determined for a series of gratings with groove densities of 1000–2400 ln mm^{-1}, where the incidence and diffraction angles are almost equally distributed around the Littrow angle θ_{Litt} (figure 2(a), left-axis), and the angular distribution of the diffraction beam (light-blue area in the figure) is due to the intra-band chromatic dispersion of the laser pulse; the calculated values of 'f_1/f_2' decreases monotonously with the groove density (right axis). More specifically, the lower groove density (e.g. 1000 ln mm^{-1}) would require higher de-magnification ($f_1/f_2 > 10$), leading to asymmetrically un-balanced optical layout; while the higher groove density (e.g. 2000 ln mm^{-1}) could satisfy reasonably lower de-magnification coupling ($f_1/f_2 \sim 4$).

The effective beam size in LN crystal could be calculated (σ_0 is the beam size before the grating),

$$\sigma_{\mathrm{LN}} = \frac{\sigma_0}{\cos\theta_{\mathrm{LN}}}\frac{\cos\beta_1}{\cos\beta_0}\frac{\cos\theta_t}{\cos\theta_i}\frac{f_2}{f_1}. \tag{7}$$

Then the laser beam fluencies are calculated and plot in figure 2(b), for various gratings and within the laser pulse energy in the range of 0.1–2 mJ. Clearly at each laser pulse energy, the beam fluence is expected to decrease along with the increasing of the grating groove density, consistent with the 'f_1/f_2' feature in figure 2(a). The 2200 ln mm^{-1} grating is eventually selected for the experiment, with f_1/f_2 of ~3 and moderate driving beam fluencies in LN (0.2–5 mJ cm^{-2}). According to previous reports, the optimal driving beam fluence of the femtosecond laser is claimed to be within the range of 1–10 mJ cm^{-2}, which is not only below the damage threshold of the LN crystal, but also smaller than the THz saturation regime to avoid the strong THz absorption from the laser induced extra free-carriers [13, 17, 19, 25].

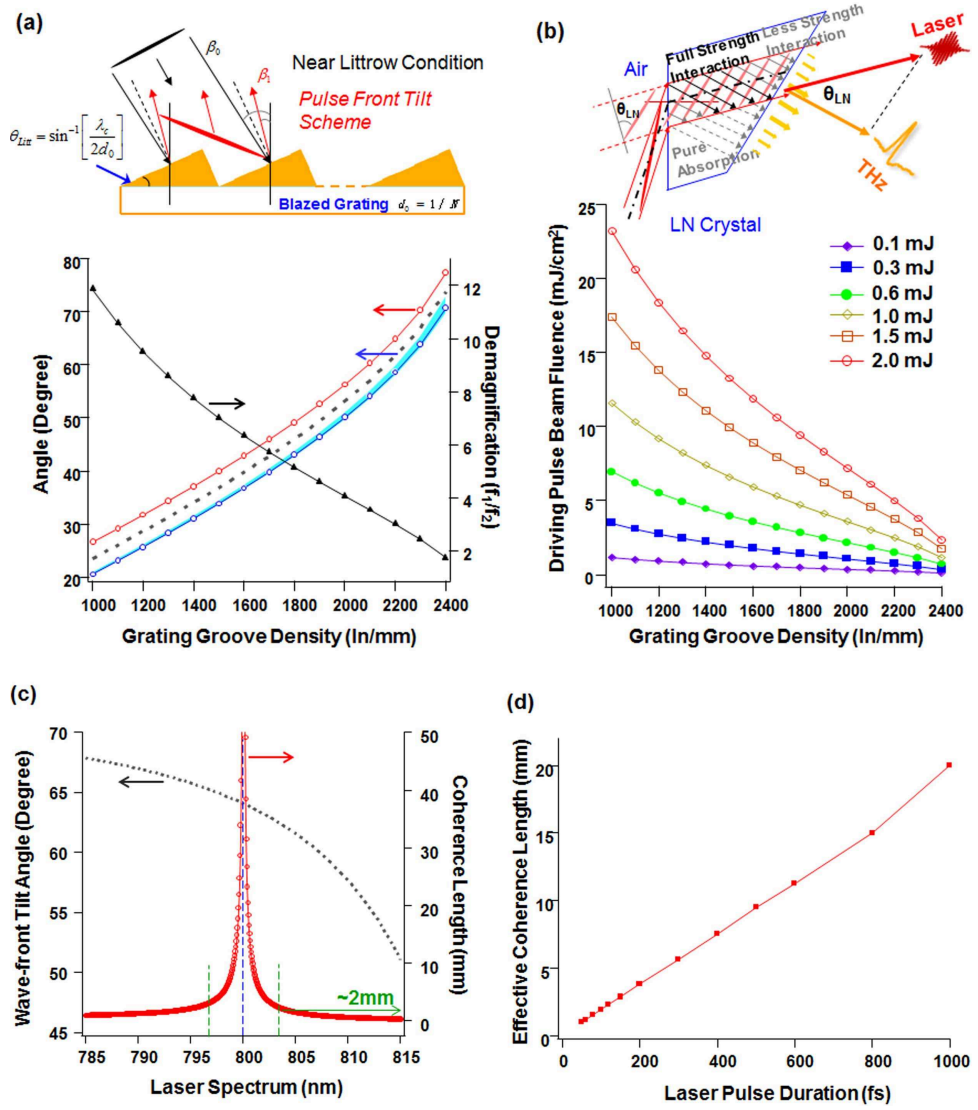

Figure 2. (a) Illustrates the pulse-front tilt generation for the laser beam through a blazed grating, with blazed angle equal to the 'Littrow' angle θ_{Litt} for the central wavelength λ_c. The incidence beam approaches the Littrow condition for high diffraction efficiency, and a few degrees' deviation from the Littrow angle could avoid spatial overlapping between the incidence/diffraction beams. The proposed 'Incidence' (red-circle-line) and 'Diffraction' (blue-circle-line) angles, distributed near to the Littrow angles (gray-dashed-line) for a series of blazed gratings with groove densities in the range of 1000–2400 ln mm^{-1} (left axis). The shadow domain (light-blue) displays the angular distribution of the 'Diffraction' beam due to the intra-band chromatic dispersion of the driving pulse. The optimal demagnification coupling of the lens-pair (refer to figure 1) f_1/f_2 (filled black-triangle, right axis) in the THz generation setup is selected to achieve the phase match in the LN crystal for the series of gratings at this geometry (see text). (b) The expectation values of the driving pulse fluence for laser pulse energy in the range of 0.1–2.0 mJ, using the same series of gratings in (a). The inserted schematic diagram above demonstrates the pulse-front tilted driving pulse penetration and interaction with the LN crystal to generate THz wave, whose transverse intensity distribution is due to the variety of the THz interaction path lengths with the laser wave-packet. (c) For the grating with groove density of 2200 ln mm^{-1} and driving laser intra-bandwidth of 7.6 nm at ~800 nm, the distribution of the pulse-front-tilt angles for specific wavelengths in LN, with respect to the central wavelength (dot-line, left-axis), where the optimal phase-match angle is ~64°; and the coherence length for THz generation (circle-line, right axis), where the two short vertical dashed lines indicate the intra-band angular dispersion would lead to the declining of the THz coherence generation length down to ~2 mm in the experiment. (d) The plot of expected 'effective coherence length' for THz generation versus the TL 'pulse length' of the driving laser for the system, where the TL intra-band distribution of each driving pulse is concerned, then the corresponding chromatic dispersion, pulse-front tilt distribution and coherence generation length can be calculated according to equations (8)–(10).

While the laser wave-packet passes through the dispersive elements of the THz system, the chromatic dispersion and angular distribution of the ultrafast pulse need to be assessed, where the different colors in the laser spectrum would incident on the LN crystal with slightly different angles, causing the deviation of the actual pulse-front tilts from the perfect phase match angle. This would lead to the declining of THz generation coherence length and the generation efficiency as well. According to figure 1(b), the incidence angle distribution at the air–LN interface $\Delta\theta_i(\lambda)$ originates from the diffraction grating, where $\Delta\beta_i(\lambda)$ propagates through CL_1 and CL_2 experiencing double refocusing, and turns into $\Delta\theta_i(\lambda) \approx \dfrac{f_1}{f_2}\Delta\beta_i(\lambda)$ at the para-axial approximation,

then

$$\theta_i(\lambda) \approx \theta_B + \Delta\theta_i(\lambda) = \theta_B + \frac{(\lambda - \lambda_c)}{d_0 \frac{f_2}{f_1}\sqrt{1 - \left(\frac{\lambda}{d_0} - \sin\beta_0\right)^2}}. \quad (8)$$

From (5), (6), (8) and Snell's law, finally we got

$$\tan\theta_{LN}(\lambda) = \frac{\lambda}{d_0 \frac{f_2}{f_1}\sqrt{1 - \left(\frac{\lambda}{d_0} - \sin\beta_0\right)^2}} \frac{n_f(\lambda)}{n_g(\lambda)} \frac{\sqrt{1 - (\sin\theta_i(\lambda))^2}}{\sqrt{n_f(\lambda)^2 - (\sin\theta_i(\lambda))^2}}, \quad (9)$$

where the optimal phase-match condition is presumably set at λ_c, and $n_f(\lambda)$ or $n_g(\lambda)$ represents the laser phase or group index in LN. The effective THz generation coherence lengths at various intra-band wave-lengths of the driving laser could be evaluated by [30]:

$$L_{coh}(\lambda) = \frac{2\pi}{\Delta k(\lambda)} \approx \lambda_{THz}\left[\frac{1}{n_{THz}(\lambda_{THz})\cos\theta_{LN}(\lambda) - n_g(\lambda)}\right]. \quad (10)$$

In figure 2(c), the calculated pulse-front tilt angle (left-axis) and corresponding THz generation coherence length (right-axis), indicate that the de-coherence for THz generation is mainly caused by the pulse-front tilt deviation from the ideal phase match due to the broadband feature of the driving pulse to induce chromatic angular distribution. For a TL driving pulse duration of ~130 fs, associated with a FWHM bandwidth of ~7.6 nm, the effective coherent length for THz generation is roughly about ~2 mm. Figure 2(d) plots a series of THz generation coherence length by applying various full coherence driving pulse durations from ~50 fs up to ~1 ps, where the curve exhibits that the coherent length is less than 2 mm for using driving pulse length of <100 fs, but beyond 10 mm for using pulse width of >500 fs [30].

2.3. Optimal driving pulse duration and THz generation length

In the previous section, the correlation between 'coherence length for THz generation' and 'driving pulse duration' is investigated; it seems that a longer pulse is more favorable in THz generation, since a short pulse associated with broader TL bandwith causes larger chromatic dispersion and angular distribution, which limits the THz generation. In fact, however, the optimal driving pulse is certainly not as long as possible, since the THz wave originates from the intra-band cascaded DFG process, a bandwidth spanning would be a prerequisite to initialize the DFG reaction chain. Typically the DFG conversion efficiency is proportional to the peak intensity of the driving laser in linear conversion region before achieving saturation. So the optimal driving pulse duration should be determined through compromising these two competitive directions [30]. In the meantime, the THz absorption in the generation media should also be considered, particularly the driving pulse induced free-carriers are expected to absorb the THz wave substantially. In our experiment, we only apply moderate driving beam fluence of a few mJ cm^{-2} to avoid saturation and carrier-induced absorption. The conversion efficiency could be numerically simulated by,

$$\eta_{THz} = \frac{2\Omega_{THz}^2 d_{eff}^2 L_{THz}^2}{\varepsilon_0 n(\omega_L)^2 n(\Omega_{THz}) c^3} \frac{F}{\tau} \frac{\sin^2[\Delta k(\tau)\cdot L_{THz}/2]}{[\Delta k(\tau)\cdot L_{THz}/2]^2} \exp[-\alpha_{THz} L_{THz}] G(L_{THz}, \tau), \quad (11)$$

where the phase matching condition, driving pulse intensity, THz absorption and geometric coupling etc are all inclusive [27]: d_{eff} is the nonlinear coefficient for THz generation in LN, $n(\omega_L)$ and $n(\Omega_{THz})$ are the phase index of the laser and THz in LN respectively, Δk is the wave-vector mis-match for these two waves (which is correlated to driving pulse duration τ as previous discussion), L_{THz} is THz generation length in the crystal, α_{THz} is the THz absorption coefficient, F is the driving beam fluence (which divided by τ is equal to the beam peak intensity), and $G(L_{THz}, \tau)$ is the geometric coupling function for the laser and THz beams (which is dependent with pulse-front tilt geometry, L_{THz} and τ).

Utilizing the parameters in our setup and pulse-front tilt scheme, a series of simulated figures demonstrating 'THz conversion efficiency'—η versus 'driving pulse duration'—τ and 'THz generation length'—L_{THz}, for several typical 'THz absorption coefficients'—α_{THz} are plot in figure 3, where the extreme conversion efficiencies for various α_{THz} are quite different, associated with diversified optimal driving pulse lengths and THz generation lengths. If α_{THz} is ~5 cm^{-1}, the optimal driving pulse duration is a bit below 100 fs, the corresponding optimal THz generation length is 1–2 mm, and the highest THz conversion efficiency is around

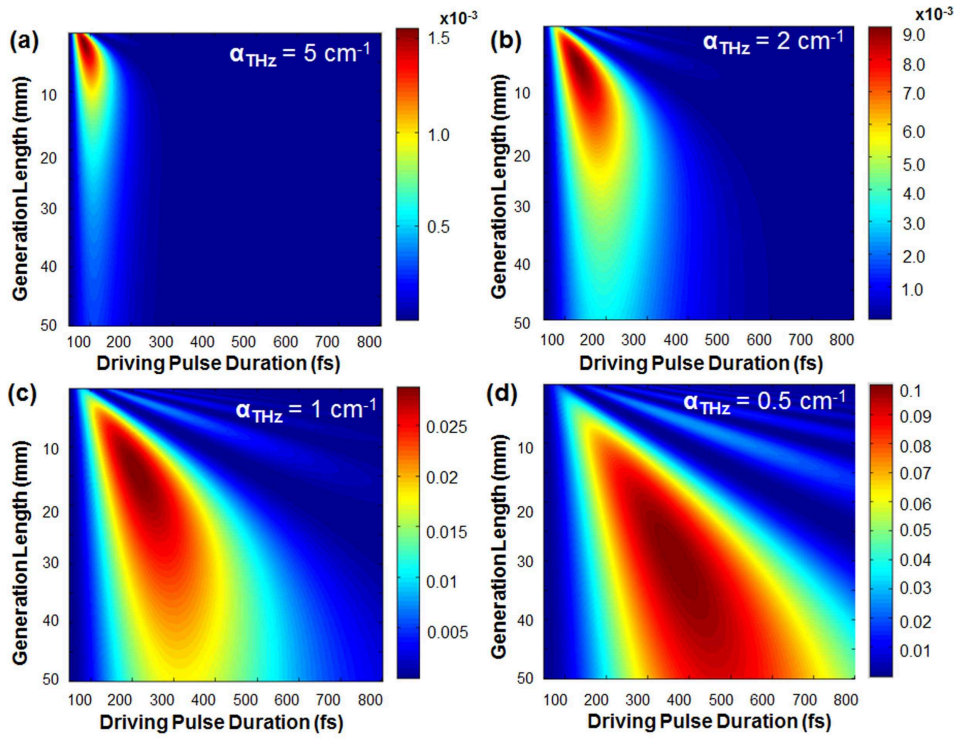

(e)

α_{THz} [cm^{-1}]	τ Pulse Duration [fs]	L_{THz} [mm]	η
0.5	~380	~31	~10.0%
1.0	~215	~14	~2.80%
2.0	~140	~7	~0.90%
5.0	~85	~2	~0.15%

Figure 3. The simulated THz generation efficiency for various transform-limit 'driving pulse duration' (τ) and 'THz generation length' (L_{THz}), at different 'THz absorption coefficients' (α_{THz}) of the crystal: (a) $\alpha_{THz} = 5.0$ cm^{-1}, (b) $\alpha_{THz} = 2.0$ cm^{-1}, (c) $\alpha_{THz} = 1.0$ cm^{-1}, (d) $\alpha_{THz} = 0.5$ cm^{-1}. In each diagram, the absolute values of the 'THz conversion efficiency distribution' in LN crystal are denoted by the color-bar. (e) The retrieved parameters for optimal THz generation at various THz absorption coefficients α_{THz} in (a)–(d), the specific τ and L_{THz} are associated with the 'extreme conversion efficiencies' (η) for each case.

~0.15% (figure 3(a)), which is quite consistent with the previous reports for deriving THz wave by ~100 fs pulse in LN at room temperature [26, 28]. If α_{THz} decreases one order less to ~0.5 cm^{-1}, the optimal pulse length should be around ~400 fs, with THz generation length beyond 30 mm, more remarkably the extreme conversion efficiency is expected to be ~10% (figure 3(d)).

During the past few years, cryogenic apparatus were proposed and developed for THz generation, which could enhance the generation efficiency enormously because the absorption is much smaller compared to that at room temperature [24, 29, 30]. In that circumstance, an extra-large size pulse-front tilted driving beam with high pulse energy and long pulse duration (to maintain the beam fluence within a few mJ cm^{-2}) should be applied to a cryogenic LN crystal with dimensions of few tens of mm, to achieve the desired THz conversion efficiency of a few percent. Currently one of the prevalent views for THz generation in LN through pulse-front-tilt scheme is that the optimal driving pulse length should be in the range of 300–500 fs unconditionally [20, 21, 24, 25]. However our investigation unveiled a different feature: the absorption coefficient of the media actually plays an essential role, and the optimal driving pulse length starts from ~400 fs for small absorption coefficient (α_{THz}~0.5 cm^{-1}), decreases down to <100 fs for large absorption coefficient (α_{THz}~5.0 cm^{-1}), while the optimal THz generation length and conversion efficiency decline 1–2 orders associatively. This could also well interpret previously unexpected experimental results at room temperature, where the THz conversion efficiency at the identical driving beam fluence decreases monotonously along with an increase of the pulse length, contradictory to the predicted optimal pulse length in the range of 300–500 fs [19, 26, 28, 31]. The optimal parameters for THz generation at various absorption coefficients are retrieved and summarized in the table of figure 3(e) for comparison.

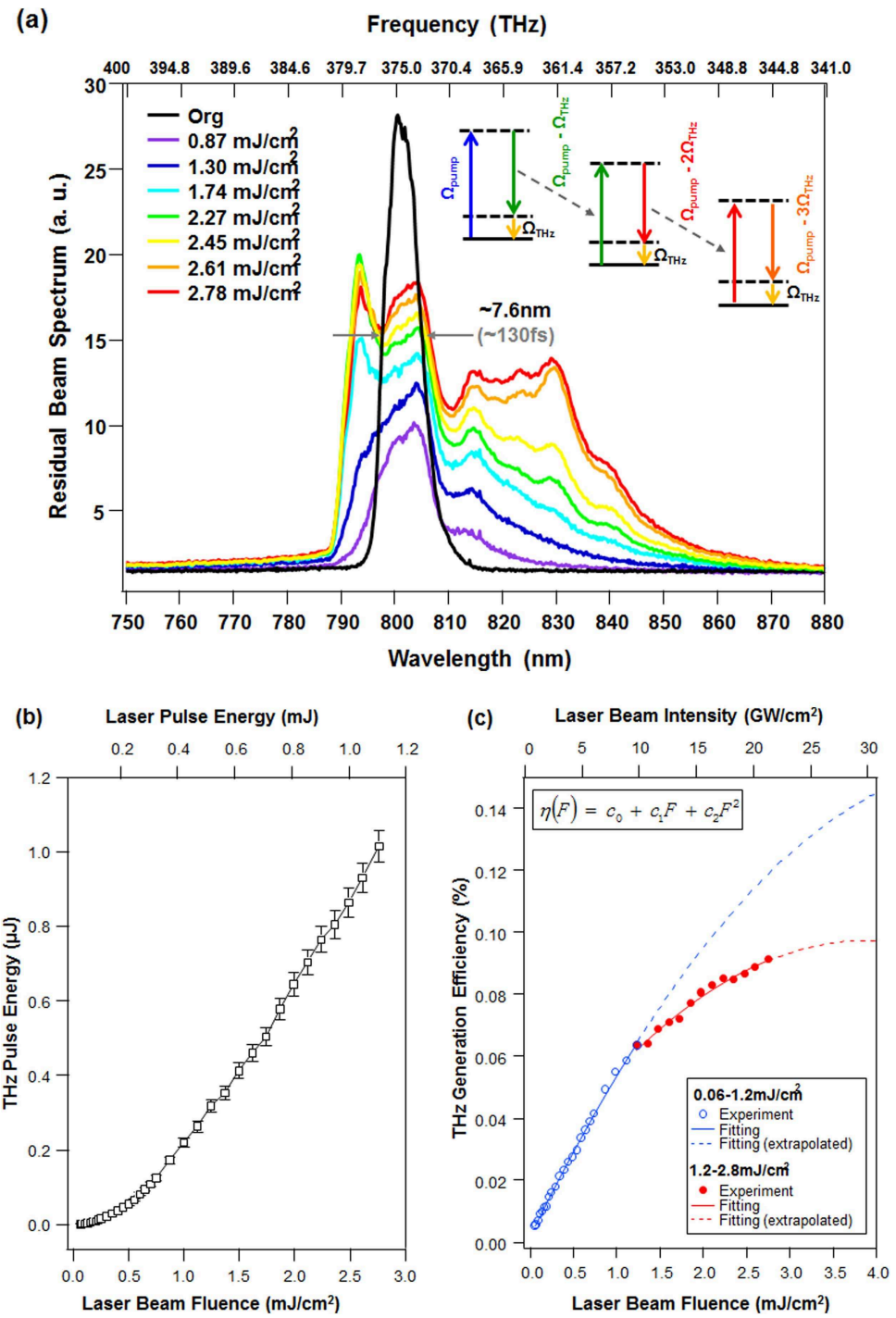

Figure 4. (a) The 'red-shift' broadening of the residual spectra of the driving laser for the THz generation in LN, at various beam fluencies. The black one is the original laser spectrum as the control signal. The inserted diagram shows that the THz generation in LN via multi-stage cascaded DFG process is causing the spectral broadening feature. (b) The THz pulse energy generated in the experiment by applying different laser beam fluencies in the range of 0.06–2.8 mJ cm^{-2} (associated with the laser pulse energy of 0.025–1.16 mJ, top-axis). The error bar in each data point indicates that the uncertainty for charactering the THz pulse energy is less than 5%. (c) The corresponding THz generation efficiency, calculated by using experimental data in (b). The domains of the low (open-circle) and high (filled-circle) beam fluencies could be fit by polynomials of second order (blue and red solid-lines), achieving two sets of parameters (in table 1). The dash curves in specified colors are the extrapolated features of the polynomials for these two specific domains (see text).

3. Results and discussion

3.1. IR residual spectra red-shift due to cascaded DFG and THz pulse generation in nonlinear conversion regime

The typical residual spectra of the driving beam fluencies in the range of 0.8−3 mJ cm^{-2} are plotted in figure 4(a). With increasing of the beam fluence, the spectra display significant 'red-shift' broadening features

Table 1. Fitting parameters for THz conversion efficiency.

Coefficient	c_0	c_1	c_2
	Unit of coefficients		
Driving beam fluence (mJ cm^{-2})	(%)	(cm^2 mJ^{-1})	(cm^4 (mJ)$^{-2}$)
0.6–1.2	$1.53 \times 10^{-3} \pm 4.6 \times 10^{-4}$	$5.74 \times 10^{-2} \pm 1.92 \times 10^{-3}$	$-5.40 \times 10^{-3} \pm 1.5 \times 10^{-3}$
1.2–2.8	$2.13 \times 10^{-2} \pm 7.0 \times 10^{-3}$	$3.90 \times 10^{-2} \pm 7.27 \times 10^{-3}$	$-5.01 \times 10^{-3} \pm 1.81 \times 10^{-3}$

(usually appointed to the signature of 'optical-to-THz' conversion with high efficiency). However when the beam fluence increases to beyond 2.5 mJ cm^{-2}, the trend of spectral 'red-shift' broadening slows down, indicating the saturation of the THz generation. As illustrated in the inserted diagram, the THz wave is generated through multi-stage cascaded DFG in the crystal, where an optical photon could convert into multiple THz photons through this frequency rolling down process, with conversion efficiency much higher than the 'Manley–Rowe limit' (only converts into a single THz photon along with another optical photon of a small red-shift [24]).

With the driving beam fluence in the range of 0.06–3 mJ cm^{-2} (corresponding to the laser pulse energy of 0.015–1.2 mJ), the generated THz pulse energy is from a few nano-Joules (nJ) up to micro-Joule (μJ) level (refer to figure 4(b)). The correlation of 'optical-to-THz conversion efficiency' versus 'laser beam fluence' is plotted in figure 4(c), and the efficiency is monotonously increasing and achieves ~0.09% at the highest beam fluence in the experiment, however when the fluence is beyond ~1.2 mJ cm^{-2}, the THz generation goes gradually towards saturation. The corresponding laser beam intensity is also given on the top axis of figure 4(c) for the TL pulse duration of ~130 fs. The experimental results of THz generation efficiency could be fitted by a polynomial of $\eta(F) = c_0 + c_1{}^*F + c_2{}^*F^2 + \cdots$ (where F and η are the laser beam fluence and THz generation efficiency, and c_j are the fitting coefficients), within two separated sections of the beam fluence, (i) 0.06–1.2 mJ cm^{-2}, and (ii) 1.2–2.8 mJ cm^{-2}. The fitting parameters for these two sections are given in table 1, where $c_1{}^*F \gg c_2{}^*F^2 \gg c_0$ implicates the THz generation is approximately in the linear conversion regime; c_2 is negative for the second order polynomial, so the maximal THz generation efficiency is expected to achieve at $F \approx -c_1/2c_2$; and c_0 represents any pseudo-effect during the process (e.g. scattering). This simple scheme would lead to the highest conversion efficiency of 0.15% at the extrapolated fluence of ~5.32 mJ cm^{-2}, for the lower beam fluence range (0.06–1.2 mJ cm^{-2}); and to the conversion efficiency of 0.097% at ~3.90 mJ cm^{-2}, for the higher beam fluence range (1.2–2.8 mJ cm^{-2}). Both are clearly demonstrated by the extrapolated dashed-curves in the plot (figure 4(c)). When the beam fluence is high, it would induce plasma distribution (or free carriers) in the crystal, which causes strong absorption of the THz wave; in the meantime, the plasma would lead to transient change of the refractive index of the media which potentially perturbs the phase match condition. So the attempt to enhance the THz generation efficiency via further increasing the driving beam fluence would be severely restricted, i.e. impossible. The saturated driving beam fluence (corresponding to where the THz generation efficiency in the experiment is maximal) is expected to be somewhere inbetween the extrapolated values obtained from the 'low' or 'high' fluence regions. In figure 4(a), the overwhelmed 'red-shift' broadening feature is actually companied by 'blue-shift', mediated by the laser-induced phase-modulation and broadband emission. And a direct comparison between the saturation trend for driving fluence of ~2.5 mJ cm^{-2} in the residual spectra (figure 4(a)) and that of ~1.2 mJ cm^{-2} in the THz generation efficiency curve (figure 4(c)), clearly shows that the 'red-shift' broadening spectra should be related to not only THz generation, but also laser plasma as well. According to the analytic scheme described here, the highest achievable THz generation efficiency in LN at room temperature by utilizing our apparatus and driving pulse length of ~130 fs would be around ~0.1%, the order of magnitude agrees with the feature predicted by figure 3(a) well.

3.2. THz time-domain waveforms derived by chirp pulses and the chirp influence on the THz generation efficiency

The experimental EO signals representing typical THz fields in time domain along with its Fourier transformations in frequency domain are displayed in figures 5(a) and (b) respectively, where the laser beam fluence of ~2.5 mJ cm^{-2} is used to derive THz wave in LN. The generated THz spectrum spans from ~0.1 THz up to ~1.5 THz, with peak strength at 300–400 GHz. Then the driving pulse is stretched to chirp pulse to derive the THz wave.

Figure 5 compares the normalized THz fields derived by TL pulse of 130 fs and by chirp pulses of 250 fs, −320 fs in pulse length (where the positive or negative sign represents the positive or negative chirp). Apparently

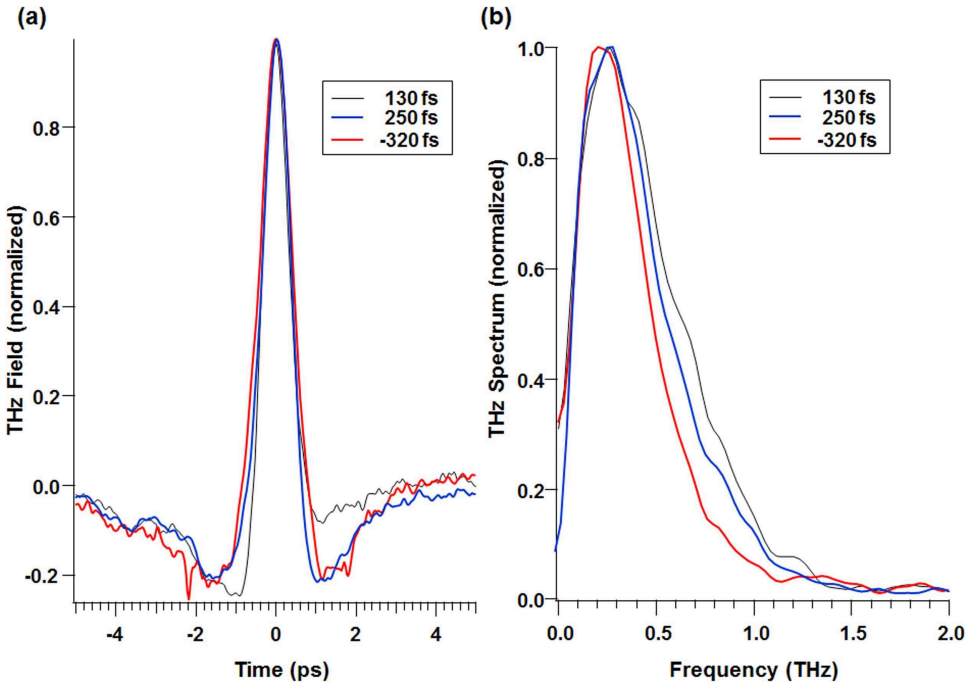

Figure 5. (a) The measured THz waveform in time-domain by electric optic sampling; the thin black curve is generated by the transform-limit driving pulse of 130 fs, and the blue and red lines by positive chirp pulse of 250 fs and negative pulse of −320 fs respectively. (b) The corresponding THz spectra in frequency-domain, via Fourier transformation of (a).

the THz waveforms generated by chirp pulses (250 fs or −320 fs) are longer than that by TL pulse, corresponding to a narrower THz spectrum (where the generated THz wave is assumed to be close to full coherence).

The different chirp pulses are generated through slightly deteriorating the optimal compensation of the pulse compressor in the laser system, and the influence of the chirp on the THz conversion efficiency is investigated. The pulse length is on-line characterized by a single shot auto-correlator (Coherent Inc., USA) via splitting few percent of the driving beam. For the linear chirp pulse, the general formula for the electric field could be expressed as,

$$E_N(t) = E_0 \mathrm{e}^{-|a_N|t^2} \cos(\omega_c t + b_N t^2), \tag{12}$$

where $\omega_c = 2\pi\dfrac{c}{\lambda_c}$ is the carrier frequency of the laser (at the central wavelength), coefficient a_N and b_N are related to the envelope duration and the linear chirp for the laser field respectively. In terms of TL pulse duration of FWHM τ_{FWHM} and pulse stretch multiple N (the ratio of chirp pulse length divided by TL pulse length, sign included), we have [32],

$$a_N = \mathrm{sign}(N) 2 \ln 2 / \tau_{\mathrm{FWHM}}^2 N^2, \tag{13.1}$$

$$b_N = a_N \sqrt{N^2 - 1}, \tag{13.2}$$

$$1/\sqrt{|a_N|}^S = \mathrm{sign}(N)/\sqrt{|a_N|}. \tag{13.3}$$

Implementing the experimental chirp pulse parameters (figure 6(c)) into equations (12), (13), the normalized field envelopes of the TL pulse of 130 fs (green), negative chirp pulse of −475 fs (red, $N = -3.65$) and positive chirp of 408 fs (blue, $N = 3.14$) are plotted together in figure 6(a). Particularly within a time window of '70–130' fs respected to the peak field of the laser (semi-transparent bar area in the figure), the 'zoomed-in' features of the field at the neighborhood of intra-pulse time scale of 70, 100 and 130 fs are highlighted for the three above pulses (figure 6(b)). Obviously the TL pulse decays much faster than the chirp pulses, while their phase differences are discernable and increasing when the intra-pulse time is further away from the peak field.

The THz generation efficiency is systematically investigated for various chirped driving pulses while maintaining the pulse fluence as a constant at ~2.5 mJ cm^{-2}. As demonstrated in figure 7, a surprisingly asymmetric curve of 'THz conversion efficiency' versus 'chirp' is observed, where the signed inverse square root of the absolute value of a_N (equation (13.3)) is used to denote the chirp magnitude. And the highest conversion

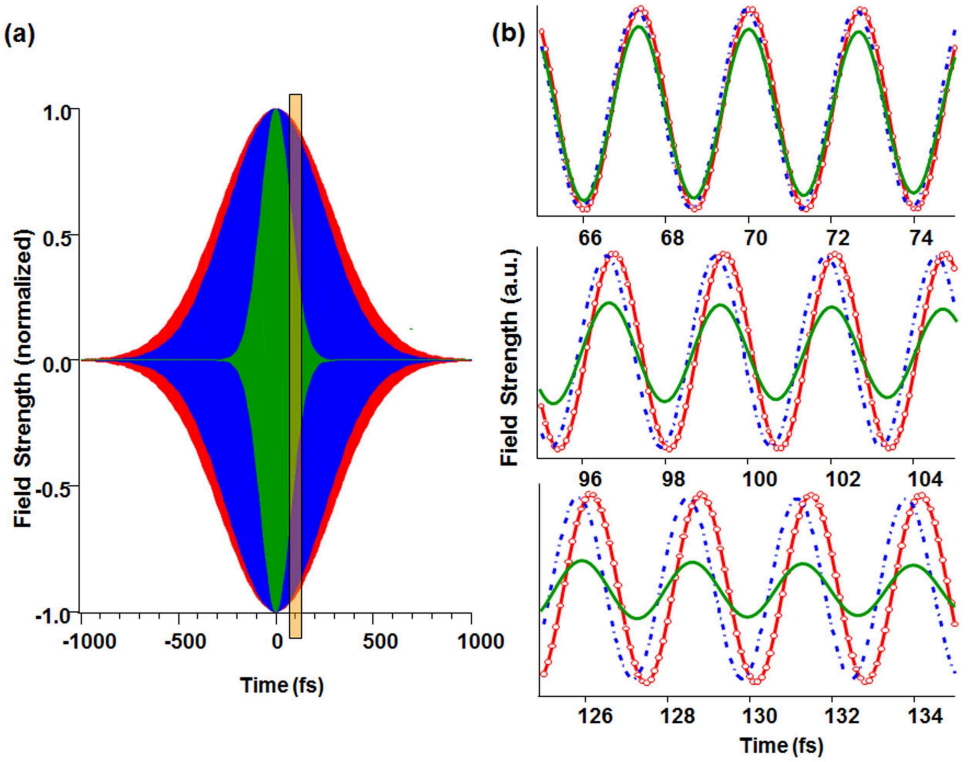

(c)

Parameters	Pulse length stretch multiples, "N"	a_N [fs^{-2}]	b_N [fs^{-2}]
Negative Chirp	-3.65	-6.153E-6	-2.161E-5
	-1.47	-3.821E-5	- 4.092E-5
Chirp Free	±1.00	±8.203E-5	0
Positive Chirp	1.10	6.866E-5	3.030E-5
	1.33	4.668E-5	4.062E-5
	1.67	2.926E-5	3.929E-5
	1.74	2.696E-5	3.853E-5
	2.07	1.915E-5	3.470E-5
	3.14	**8.322E-6**	**2.477E-5**
	6.22	2.120E-6	1.301E-5

Figure 6. (a) The simulated driving pulse waveforms (normalized) for TL pulse duration of 130 fs (green), negative chirp pulse duration of −475 fs (red), and positive chirp pulse duration of 408 fs (blue) used in the experiment. The vertically semi-transparent bar area across the three wave-packets represents a time-window of (65, 135) fs with respect to the field peak. (b) 'Zoomed-in' views for three typical '10-fs' sub-windows within the '65–135 fs' window (the central time scales of the three sub-windows are 70, 100, 130 fs with respect to the field peak) and comparison of the electric fields of the three normalized pulses, demonstrate the phases of negative (red circle-line) and positive (blue dot-line) chirp pulses are shifting oppositely respected to the chirp-free pulse (green solid-line). (c) Parameters for various chirp pulses used in the experiment, and in part (a) '−475 fs' corresponds to '$N = -3.65$', and '408 fs' corresponds to '$N = 3.14$' in the table.

efficiency is achieved at a positive chirp value, not at the TL pulse. Especially when the driving pulse length is approaching to TL duration, the THz conversion becomes pretty low instead, but immediately increases to one order higher when positive chirps are applied; for negative chirps, the growth rate of the curve is moderated, associated with much smaller generation efficiency. With further stretching the pulse duration, the THz generation efficiency gradually decreases and becomes more or less balanced for both sides of the chirp. The longest chirp pulse durations in the experiment are −475 fs and 808 fs for the negative and positive chirps respectively, due to the limit of the motor travel range of the pulse compressor [30, 33].

3.3. More discussions regarding to THz generation using chirp driving pulses

We developed a theoretical model to investigate the unexpected phenomenon of chirp asymmetry for the THz generation. Utilizing of the DFG simulation strategy in pulse-front tilt scheme, we have,

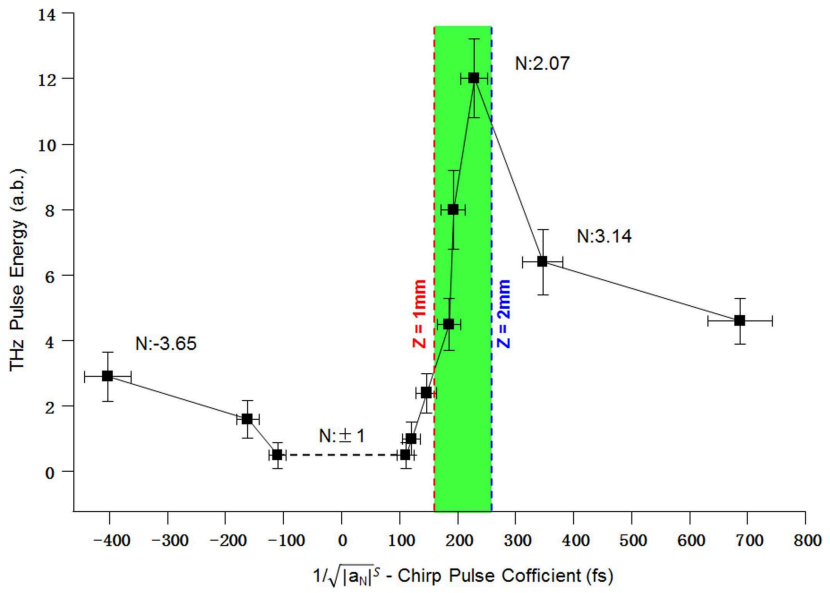

Figure 7. The THz pulse energy generated by using identical driving beam fluence of ~2.5 mJ cm^{-2}, while the chirp of the pulse is changed from negative, to chirp-free (corresponding to the transform-limit pulse), and then to positive. A few typical stretching multiples '*N*' from the experiment are highlighted near to their corresponding data points. The two vertical dash lines and enclosed bar-area represent the spanning range of the calculated chirp pulse coefficients $1/\sqrt{|a_N|}^{S(\mathrm{OPT})}$ for the optimal THz conversion efficiency within the generation length range of 1–2 mm, according to equation (19). Obviously the optimal stretching multiple $N^{(\mathrm{OPT})}$ ~2.07 (associated with the highest THz generation efficiency in the experiment) is well located within the region (see text).

$$\begin{aligned}
&\int_{-\infty}^{+\infty} \mathrm{d}\omega' \tilde{E}_L(r,\omega')\tilde{E}_L^*(r,\omega'-\omega+\Omega_{\mathrm{THz}})\mathrm{e}^{-\mathrm{i}k_{\mathrm{THz}}\cdot r}\\
&\quad=\int_{-\infty}^{+\infty} \mathrm{d}\omega' |\tilde{E}_L(r,\omega')|\ \mathrm{e}^{\mathrm{i}\varphi(\omega')}|\tilde{E}_L^*(r,\omega'-\omega+\Omega_{\mathrm{THz}})|\ \mathrm{e}^{-\mathrm{i}\varphi(\omega'-\omega+\Omega_{\mathrm{THz}})}\mathrm{e}^{-\mathrm{i}k_{\mathrm{THz}}\cdot r}\\
&\quad\approx\int_{-\infty}^{+\infty} \mathrm{d}\omega' |\tilde{E}_L(r,\omega')|^2{}_{\omega=0}\mathrm{e}^{\mathrm{i}\varphi(\omega')-\mathrm{i}\varphi(\omega'-\omega+\Omega_{\mathrm{THz}})}\mathrm{e}^{-\mathrm{i}k_{\mathrm{THz}}\cdot r}\\
&\quad\approx\int_{-\infty}^{+\infty} \mathrm{d}\omega' |\tilde{E}_L(r,\omega')|^2{}_{\omega=0}\mathrm{e}^{-\mathrm{i}\frac{\partial\varphi}{\partial\omega}\Omega_{\mathrm{THz}}}\mathrm{e}^{-\mathrm{i}k_{\mathrm{THz}}\cdot r}.
\end{aligned}\tag{14}$$

The phase factor of equation (14) could be evaluated as the 'ω' terms in various orders,

$$\begin{aligned}
&-\frac{\partial\varphi(\omega)}{\partial\omega}\Omega_{\mathrm{THz}}-k_{\mathrm{THz}}\cdot r\approx -2b_\omega\omega\cdot\Omega_{\mathrm{THz}}-k_{\mathrm{THz}}\cdot r\\
&\quad-\frac{z\cdot\Omega_{\mathrm{THz}}}{k_L c^2}n(\omega-\omega_L)\left[n+\frac{\partial n}{\partial\omega}(\omega-\omega_L)\right]\\
&=\frac{r\cdot\Omega_{\mathrm{THz}}}{c}\left(n-\frac{\partial n}{\partial\omega}\omega_L\right)-\frac{z\cdot\Omega_{\mathrm{THz}}}{c}n(\Omega_{\mathrm{THz}})\\
&\quad+\left[-2b_\omega\Omega_{\mathrm{THz}}-\frac{z\cdot\Omega_{\mathrm{THz}}}{\omega_L c}\left(n-2\omega_L\frac{\partial n}{\partial\omega}\right)\right]\omega+\frac{z\cdot\Omega_{\mathrm{THz}}}{k_L c^2}\left(-n\frac{\partial n}{\partial\omega}\right)\omega^2+\cdots.
\end{aligned}\tag{15}$$

When the output value (absolute) of equation (15) approaches to minimum (i.e. zero), it is corresponding to the phase match condition for the highest THz conversion efficiency. Thus various orders of 'ω' terms could be analyzed separately.

(i) Zero order of ω

$$\left[r\cdot\left(n(\omega)-\frac{\partial n(\omega)}{\partial\omega}\omega_L\right)-z\cdot n(\Omega_{\mathrm{THz}})\right]\frac{\Omega_{\mathrm{THz}}}{c}=0.\tag{16.1}$$

It represents the primary phase-match condition for the THz generation, where r and z represent the travel distances of the laser and THz beams respectively. At the condition of $r = z/\cos\theta$, equation (16.1) is equivalent to the pulse-front tilt scheme described by equations (2)–(4).

(ii) First order of ω

$$b_\omega = -\frac{z}{2\omega_L c}\left(n(\omega) - 2\omega_L \frac{\partial n(\omega)}{\partial \omega}\right). \tag{16.2}$$

b_ω is defined in equation (17) later, which indicates applying a certain amount of linear chirp for the pump laser pulse would promote THz generation, and the desired linear chirp value is expected to be proportional to the THz generation length—'z' in the LN crystal.

(iii) Second order of ω and above

$$\frac{z\Omega_{\mathrm{THz}}}{k_L c^2}\left(-n(\omega)\frac{\partial n(\omega)}{\partial \omega}\right)\omega^2 + 0[\omega^3]. \tag{16.3}$$

It is related to the other nonlinear complex processes in the THz generation, e.g. laser-induced transient change of the refractive index, scattering and diffraction effect of the media etc, but its contribution to the overall phase is relatively smaller compared with the first two terms.

Concerning a Gaussian driving pulse with linear chirp, the electric field in time domain could be derived from that in frequency domain through Fourier transformation,

$$\begin{aligned} E_N(t) &= \frac{1}{\sqrt{2\pi}}\int_{-\infty}^{+\infty} E_0 \exp\left[-\frac{\omega^2}{4a_1} - \mathrm{i}b_\omega(\omega+\omega_c)^2\right]\cdot \mathrm{e}^{\mathrm{i}\omega t}\mathrm{d}\omega \\ &= \frac{1}{\sqrt{2\pi}}E_0\cdot \mathrm{e}^{-\mathrm{i}\omega_c t}\int_{-\infty}^{+\infty} \exp\left[-\frac{\omega^2}{4a_1} - \mathrm{i}b_\omega\omega^2\right]\cdot \mathrm{e}^{\mathrm{i}\omega t}\mathrm{d}\omega \\ &= E_0\cdot \mathrm{e}^{-\mathrm{i}\omega_c t}\sqrt{\frac{2a_1}{1+4\mathrm{i}a_1 b_\omega}}\,\mathrm{e}^{-\frac{a_1}{N^2}t^2}\cdot \mathrm{e}^{+4\mathrm{i}\frac{a_1^2 b_\omega}{N^2}t^2}. \end{aligned} \tag{17}$$

Here the parameter a_1 is identical to the series of a_N at $N = 1$ in equations (12), (13); b_ω represents the linear chirp parameter in frequency domain; $N = \sqrt{1+16a_1^2 b_\omega^2}$ is the same as the stretching multiple 'N' in equation (13). Relating the linear chirp phase term in equation (17) (real part) with that in equation (12), b_N in the time domain could be expressed in term of b_ω in the frequency domain,

$$b_N = -4\frac{a_1^2 b_\omega}{N^2}. \tag{18}$$

Combining equations (13), (16.2) and (18), the optimal stretching multiple for the chirp pulse, $N^{(\mathrm{OPT})}$ (where the superscript of 'OPT' denotes as the optimal value) could be determined through

$$\begin{aligned} \sqrt{(N^{(\mathrm{OPT})})^2 - 1} &= -\frac{2\ln 2}{\tau_{\mathrm{FWHM}}^2} b_\omega^{(OPT)} = \frac{z\cdot \ln 2}{\tau_{\mathrm{FWHM}}^2 \omega_L c}\left(n_L - 2\omega_L\frac{\partial n_L}{\partial \omega}\right) \\ &= \frac{z\cdot \lambda_L \cdot \ln 2}{\tau_{\mathrm{FWHM}}^2 c^2}\left(n_L + 2\lambda_L\frac{\partial n_L}{\partial \lambda}\right). \end{aligned} \tag{19}$$

Obviously $N^{(\mathrm{OPT})}$ is dependent with the THz generation length –'z' as well. Implementation the parameters in the experiment, the optimal chirp pulse stretching multiples are $N^{(\mathrm{OPT})} = 1.43$ or 2.31 for the THz generation length of 1 or 2 mm respectively, associated with the calculated value of $1/\sqrt{|a_N|}^S$ in the range of 158–255 fs. And the experimental value of $N \sim 2.07$ (i.e. $1/\sqrt{|a_N|}^{S(\mathrm{OPT})}$~228 fs) for the optimal THz conversion efficiency is well located inside this regime (refer to figure 7).

Since the laser pulse fluence of ~2.5 mJ cm^{-2} used in the experiment is beyond the THz linear conversion region, the conversion efficiency is relatively low at the TL pulse duration. And application of the positive chirp for the driving pulse would promote the THz conversion efficiency dramatically. Since the chirp parameters e.g. a_N, b_N are assigned values, the positive and negative values exhibit completely different features for satisfying the optimal THz generation condition (i.e. equation (19) is only valid for the positive 'N', but not for the negative one), so the chirp asymmetry behavior is sensible [30, 33].

4. Conclusion

Here we developed a novel THz generation apparatus by utilizing a unique 'dual-face-cut' LN crystal in Brewster's incidence geometry, and experimentally demonstrated the optical-to-THz conversion efficiency of ~0.1% could be achieved at room temperature by using a conventional Ti:Sapphire laser (~800 nm) with pulse length of ~130 fs. Since the material chromatic dispersion of LN in the neighborhood of the driving wavelength is small, our THz generation scheme could potentially be extended to broader driving wavelength range.

We systematically investigated the various determinants which restrict the THz conversion efficiency implementing pulse-front tilt scheme, and recognized that the chromatic dispersion and angular distribution are the most primary constrains for improving the THz generation length and conversion efficiency. And we found out that the THz absorption coefficient α_{THz} plays an essential role, when it decreases from ~5 cm^{-1} (at room temperature) to below ~1 cm^{-1} (probably at the cryogenic temperature), the THz conversion efficiency would be increased to more than one order higher, from ~0.1% into the level of a few percent, and the extreme conversion efficiency is predicted at ~10%. In order to achieve this, the optimal driving pulse duration should be increased from ~100 fs up to ~400 fs and the corresponding optimal THz generation length should be enhanced from 1–2 mm up to few tens of mm.

Furthermore, the influence of the chirp of the driving pulse on the THz generation efficiency is studied, for the identical driving pulse fluence of ~2.5 mJ cm^{-2} at the mild saturated region. We discovered that the positive chirp would promote much higher conversion efficiency (1 or 2 orders higher) compared to the negative chirp, exhibiting a surprising asymmetry feature in the conversion efficiency curve. A simulation script is developed to interpret this intriguing feature and reproduce the experimental results successfully, implicating that applying appropriate positive chirp for the driving pulse could potentially be a general strategy to enhance THz generation efficiency in pulse-front-tilt scheme.

According to equation (19), the chirp should be proportional to $\propto z/\tau^2_{\mathrm{FWHM}}$. The optimal THz generation length is a few tens of mm (e.g. z~31 mm), and the optimal pulse duration is ~400 fs for the small absorption coefficient case (e.g. α_{THz}~0.5 cm^{-1}), compared with ~2 mm and ~100 fs for the large absorption case (e.g. α_{THz}~5.0 cm^{-1}). Therefore the optimal stretching multiple $N^{(\mathrm{OPT})}$ for both cases should be more or less similar. And it might be quite useful for the experimental practice by using a TL pulse length in 300–400 fs to derive THz wave in a cryogenic setup, particularly it is worthwhile to generate chirps for the driving pulses and investigate experimentally that the THz generation efficiency would be enhanced as expected. Due to the lack of appropriate laser systems providing 300–400 fs TL pulses in our laboratory, currently we are not able to investigate this, but more delicate apparatus are under construction for further investigation.

Acknowledgments

The authors thank for the staff and facility support from the Department of Free Electron Laser Science & Technology and Water Science Research Center, Shanghai Institute of Applied Physics, Chinese Academy of Sciences; and support from Laboratory for High Intensity Optics, Shanghai Institute of Optics and Fine Mechanics, Chinese Academy of Sciences. The authors also appreciate the previous support and valuable discussion with Prof. Kaertner and the group at DESY, Hamburg.

Thank for the funding supports from National Science Foundation of China (grants # 11475249), and Youth 1000-Talent Program in China (grants # Y326021061).

References

[1] Liu M *et al* 2012 Terahertz-field-induced insulator-to-metal transition in vanadium dioxide metamaterial *Nature* **487** 345–8
[2] Ferguson B and Zhang X-C 2002 Materials for terahertz science and technology *Nat. Mater.* **1** 26–33
[3] Kim K Y, Taylor A J, Glownia J H and Rodrigues G 2008 Coherent control of terahertz supercontinuum generation in ultrafast laser-gas interactions *Nat. Photon.* **2** 605–9
[4] Cole B E, Williams J B, King B T, Sherwin M S and Stanley C R 2001 Coherent manipulation of semiconductor quantum bits with terahertz radiation *Nature* **410** 60–3
[5] Rini M, Tobey R, Dean N, Itatani J, Tomioka Y, Tokura Y, Schoenlein R W and Cavalleri A 2007 Control of the electronic phase of a manganite by mode-selective vibrational excitation *Nature* **449** 72–4
[6] Grguras I *et al* 2012 Ultrafast x-ray pulse characterization at free-electron lasers *Nat. Photn.* **6** 852–7
[7] Liao G-Q *et al* 2016 Demonstration of coherent terahertz transition radiation from relativistic laser-solid interactions *Phys. Rev. Lett.* **116** 205003
[8] Fruehling U *et al* Single-shot terahertz-field-driven x-ray streak camera *Nat. Photon.* **3** 523–8
[9] Daranciang D, Goodfellow J, Fuchs M, Wen H, Ghimire S, Reis D A, Loos H, Fisher A S and Lindenberg A M 2011 Single-cycle terahertz pulses with >0.2 V/A field amplitudes via coherent transition radiation *Appl. Phys. Lett.* **99** 141117
[10] Chen Z, Zhou X, Werley C A and Nelson K A 2011 Generation of high power tunable multicycle terahertz pulses *Appl. Phys. Lett.* **99** 071102
[11] Wu Q and Zhang X-C 1997 Free-space electro-optics sampling of mid-infrared pulses *Appl. Phys. Lett.* **71** 1285–6
[12] Sell A, Leitenstorfer A and Huber R 2008 Phase-locked generation and field-resolved detection of widely tunable terahertz pulses with amplitudes exceeding 100 MV/cm *Opt. Lett.* **33** 2767–9
[13] Wynne K and Carey J J 2005 An integrated description of terahertz generation through optical rectification, charge transfer, and current surge *Opt. Commun.* **256** 400–13
[14] Nahata A, Weling A S and Heinz T F 1996 A wideband coherent terahertz spectroscopy system using optical rectification electro-optic sampling *Appl. Phys. Lett.* **69** 2321–3
[15] Fraser J M and Ventalon C 2006 Parametric cascade downconverter for intense ultrafast mid-infrared generation beyond the Manley–Rowe limit *Appl. Opt.* **45** 4109–13

[16] Hattori T and Takeuchi K 2007 Simulation study on cascaded terahertz pulse generation in electro-optic crystals *Opt. Express* **15** 8076–93
[17] Volk T and Woehlecke M 2008 *Lithium Niobate* (Berlin: Springer)
[18] Yang K H, Richards P L and Shen Y R 1971 Generation of far-infrared radiation by picosecond light pulses in LiNbO3 *Appl. Phys. Lett.* **19** 320–3
[19] Yeh K-L, Hoffmann M C, Hebling J and Nelson K A 2007 Generation of 10 μJ ultrashort terahertz pulses by optical rectification *Appl. Phys. Lett.* **90** 171121
[20] Fueloep J A, Palfalvi L, Hoffmann M C and Hebling J 2011 Towards generation of mJ-level ultrashort THz pulses by optical rectification *Opt. Express* **19** 15090–7
[21] Hebling J, Yeh K-L, Hoffmann C, Bartal B and Nelson K A 2008 Generation of high-power terahertz pulses by tilted-pulse-front excitation and their application possibilities *J. Opt. Soc. Am.* B **25** B6–19
[22] Hirori H, Doi A, Blanchard F and Tanaka K 2011 Single-cycle terahertz pulses with amplitudes exceeding 1 MV/cm generated by optical rectification in LiNbO3 *Appl. Phys. Lett.* **98** 091106
[23] Hebling J, Almasi G and Kozma I Z 2002 Velocity matching by pulse front tilting for large-area THz-pulse generation *Opt. Express* **10** 1161–6
[24] Huang S-W, Granados E, Huang W R, Zapata L E and Kaertner F X 2013 High conversion efficiency, high energy terahertz pulses by optical rectification in cryogenically cooled lithium niobate *Opt. Lett.* **38** 796–8
[25] Fueloep J A, Palfalvi L, Klingebiel S, Almasi G, Krausz F, Karsch S and Hebling J 2012 Generation of sub-mJ terahertz pulses by optical rectification *Opt. Lett.* **37** 557
[26] Wu X, Carbajo S, Ravi K, Ahr F, Cirmi G, Zhou Y, Muecke O D and Kaertner F X 2014 Terahertz generation in lithium niobate driven by Ti:sapphire laser pulses and its limitations *Opt. Lett.* **39** 5403
[27] Yariv A 1988 *Quantum Electronics* 3rd edn (New York: Wiley)
[28] Jewariya M, Nagai M and Tanaka K 2009 Enhancement of terahertz wave generation by cascaded X(2) processes in LiNbO3 *J. Opt. Soc. Am.* B **26** A101–6
[29] Ravi K, Huang W R, Carbajo S, Wu X and Kaertner F 2014 Limitations to THz generation by optical rectification using tilted pulse fronts *Opt. Express* **22** 20239
[30] Fueloep J A, Palfalvi L, Almasi G and Hebling J 2010 Design of high-energy terahertz sources based on optical rectification *Opt. Express* **18** 12311–27
[31] Dorney T D, Baraniuk R G and Mittleman D M 2001 Material parameter estimation with terahertz time-domain spectroscopy *J. Opt. Soc. Am.* A **18** 1562–71
[32] Li W, Liu J, Zeng Z and Zhang Z 2003 Theoretical investigation of effect of pulse chirp on high-order harmonic spectrum *Chin. J. Lasers* **30** 509–11
[33] Bakunov M I and Bodrov S B 2014 Terahertz generation with tilted-front laser pulses in a contact-grating scheme *J. Opt. Soc. Am.* B **31** 2549